IEEE Robotics & Automation Magazine (RAM) paper, presented at ICRA 2023, London, UK. Cite as RAM paper.

Biomimetic Electric Sense-Based Localization

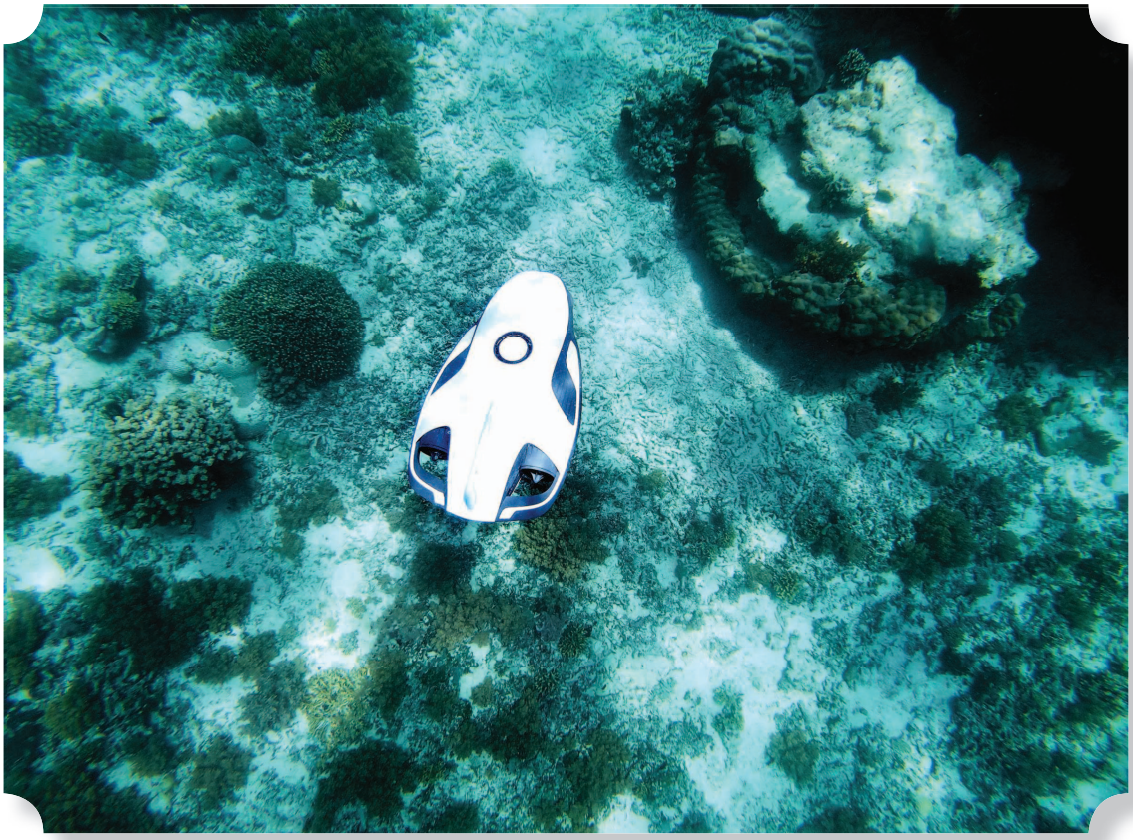

A Solution for Small Underwater Robots in a Large-Scale Environment

By Junzheng Zheng, Jingxian Wang, Xin Guo, Chayutpon Huntrakul, Chen Wang, and Guangming Xie

Digital Object Identifier 10.1109/MRA.2022.3202432
Date of current version: 22 September 2022

This article presents a novel localization scheme for free-swimming small underwater robots in a large-scale environment. Accurate localization technology has always been a challenge for small underwater robots since the underwater lighting conditions can limit their vision, while the multipath interference issue occurring near a wall plagues the sonars. By contrast, some kinds of fish perceive their positions by sensing the electric field in their environment, giving them the ability to accurately localize in underwater environments. Inspired by the electric sense behavior in fish, this article proposes a large-scale localization scheme based on electric

IEEE Robotics & Automation Magazine (RAM) paper, presented at ICRA 2023, London, UK. Cite as RAM paper.

1070-9932/22©2022IEEE

sense for small underwater robots. Our scheme includes an electric sense-based hardware solution and localization methods. Specifically, we first design a hardware solution, including electric emitters placed in an underwater environment and an electric receiver that can be furnished on a small underwater robot. Then, we propose distributed emitter architectures for large-scale localization. Finally, we propose three localization methods to estimate the position and orientation of the robot. We have conducted four types of localization experiments for a small underwater robot, demonstrating the robustness and effectiveness of our proposed electric sense-based scheme. Our study provides a novel solution to the localization of free-swimming underwater robots with a limited payload and also helps provide insights into large-scale underwater localization.

Underwater Biomimetic Perception

As one of the most popular underwater perception methods, sonar is inspired by underwater creatures, such as dolphins. Although sonars can take measurements across long distances (~2 km), they are sensitive to reflections and reverberations occurring near a wall or in turbid waters [1]. Another important underwater perception method is vision, which is informative. However, vision is more sensitive to lighting conditions and can fail in dark or turbid waters. To overcome these shortcomings, researchers and engineers keep trying to develop new technologies, especially from the perspective of bionics. In this process, the lateral line system, which has been found in many aquatic vertebrates, has attracted attention. As an important sensory system, the lateral line system is composed of mechanoreceptors and/or electroreceptors [2]. The mechanoreceptors are direction-sensitive neuromasts containing hair cells, and they are more sensitive to flow [3]. The electroreceptors are sensitive to electrical fields and have been discovered in some fish species that we call *electric fish*. Further research has revealed that electric sense is closely related to various behaviors of electric fish, such as prey, defense, perception, and communication [4]. Both kinds of receptors are suitable for turbid and dark water, and both are suitable for carrying on small underwater robots. Table 1 summarizes the advantages and disadvantages of the biomimetic perception technologies we have discussed.

Biomimetic Electric Sense in Underwater Robots

Among the various kinds of electric fish, electric eels (*Electrophorus electricus*) are well known for their powerful discharge capacity of hundreds of volts. They use these powerful electric currents for catching prey or in defense. Actually, weakly electric fish (gymnotiforms and mormyriforms) are more common in nature. They generate only about 10 V for short-distance electrolocalization and electrocommunication [4]. For some underwater creatures that have electroreceptors but cannot emit an electric field, their electric sense is used for navigation, enabling these creatures to follow the electric field generated by external electric sources (this is also called *electrotaxis*) [6].

Inspired by the weakly electric fish in nature, various underwater robots with electric sense have been designed for object estimation, localization, navigation, and so on. In 2008, Solberg et al. realized electric sense-based localization and size estimation of a sphere using a particle filter (PF) [7]. In 2015 and 2017, Bai et al. and Lanneau et al. independently realized the estimation of the pose and the shape of an ellipsoid [8], [9]. In 2013, Lebastard et al. fused the kinematic model and electric measurements to estimate the robot's pose and then used the estimated pose for navigation close to a wall [10]. In 2014, Dimble et al. modeled the electric field in a straight water tank based on the multiple mirror method and then proposed a state (lateral position and orientation) estimation method for realizing navigation in the tank [11]. In 2015, Boyer et al. designed an electric sense-based control law for their robot "Slender probes" to move toward an external electric emitter. They then activated multiple external emitters in series, creating a dynamic electric field to further realize navigation of a single robot [12]. Recently, we proposed an electric sense-based localization method for a small underwater robot, where a single electric emitter based on dc is adopted. Due to the large dc noise in the environment and the use of the single-emitter architecture, the effective sensing distance is only twice the body length of the signal emitter [13].

However, we observe that most existing electric sense-based studies are realized by dragging robots on guide rails, and there are relatively few studies based on free-swimming robots [13], [14], [15]. Also, most of the studies are focused on the localization of an external target based on a self-generated electric field [7], [8], [9], rather than the localization of the robot itself based on an external electric field.

In this article, inspired by the previous observations, we aim to design a biomimetic electric sense-based localization scheme for free-swimming underwater robots in a large-scale environment (Figure 1). To this end, we extend our previous work [13] by 1) designing an ac signal-based scheme instead of the dc one, 2) constructing the distributed electric-emitter architectures for large-scale localization, 3) exploring and analyzing the contributing factors of localization in different scenarios, and 4) verifying our localization scheme in more complex scenarios.

Table 1. Underwater biomimetic perception technologies.

Methods	Bionic Objects	Pros	Cons
Sonar [1]	Dolphin	Long distance	Big size, **turbid**, near wall
Vision [5]	Many fish	Informative	Short distance, **turbid**, **dark**
Mechano receptors [3]	Goldfish, boxfish	**Turbid**, **dark**	Short distance, Flow sensitive
Electro receptors [6]	Weakly electricfish	**Turbid, dark**	Short distance

Specifically, we propose an electric sense-based localization scheme, including a hardware solution and model-based perception methods. First, the hardware solution is composed of an ac-based electric receiver implemented on a robot and ac-based electric emitters fixed on the seabed (Figure 2). The robot uses the measurements of its receiver to estimate its relative position and orientation to the emitters on the seabed. Second, to enable localization in a large-scale environment, we construct a distributed electric-emitter architecture (Figure 3). Because an ac signal is used for localization, multiple emitters can work together without interfering with each other using frequency-division multiplexing. Then, to explore the contributing factors of localization, we design three localization methods by selectively fusing the dynamic model, inertial measurement unit (IMU), and electric sense-based measurements (Figure 4). Finally, to fully verify our proposed localization scheme, we conduct four types of localization experiments in different scenarios, including the

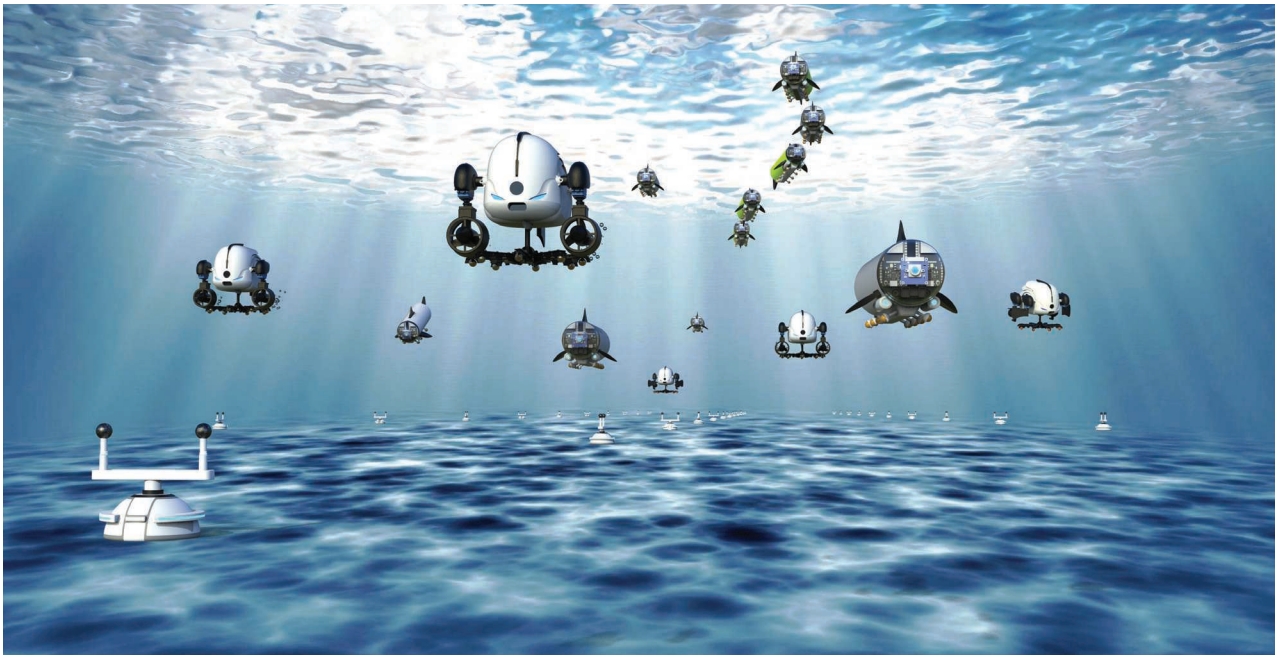

Figure 1. A concept map depicting our biomimetic electric sense-based localization framework applied to different kinds of underwater robots in the sea. The emitters are fixed on the seabed, while the receivers are equipped on the robots.

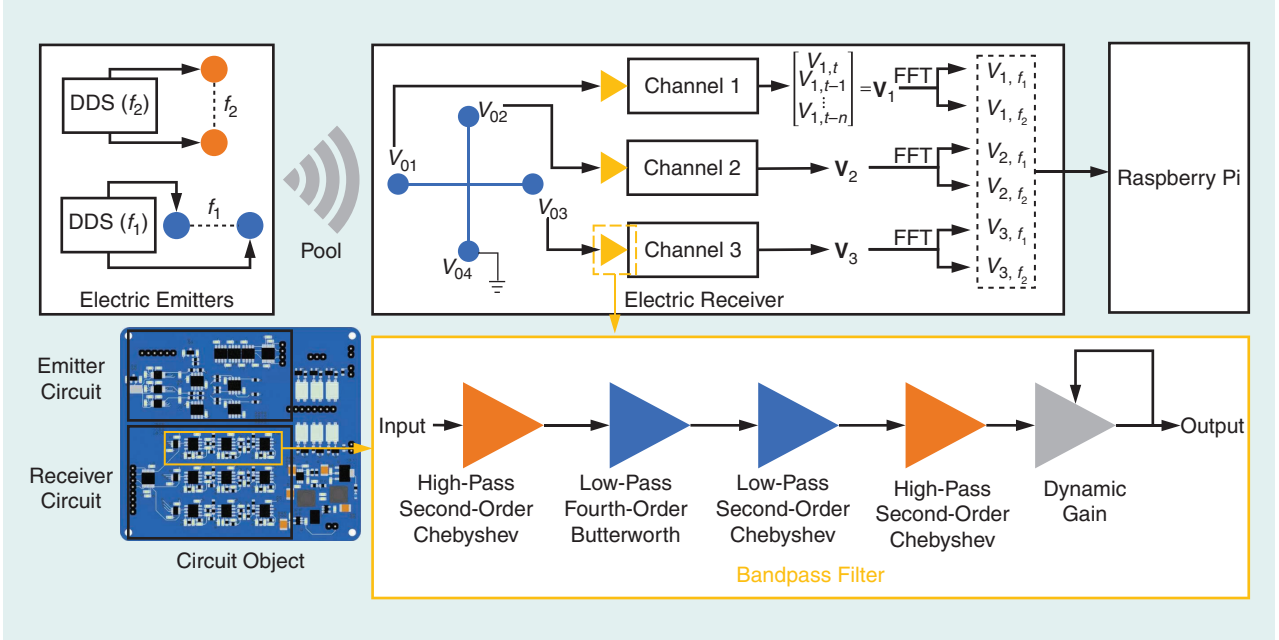

Figure 2. The hardware solution to the underwater electric sense, including the electric emitter and the electric receiver. DDS: direct digital synthesizer; FFT: fast Fourier transform.

localization of a stationary robot or a robot under towing, the position tracking problem for an autonomous swimming robot, and the kidnapped robot problem, which is much more complicated. This article may provide insights into the localization of small underwater robots in a large-scale environment and help explore the contributing factors of this new localization technology.

Our main contributions are summarized as follows.

1) We construct an electric sense-based localization scheme, including the ac-based receiver, ac-based emitters, and distributed emitter architectures. The localization scheme enables a small underwater robot to locate itself in a large-scale environment.
2) We propose three localization methods to explore the contributing factors of biomimetic electric sense-based perception. The best one is successfully applied to a more complex localization issue (the kidnapped robot problem).
3) As far as the authors are aware, few studies have considered the electric sense for free-swimming robots or the localization of the robot itself by the external electric field.

Hardware Solution to Biomimetic Electric Sense

To realize the underwater electric sense, we first design a hardware solution, including an electric emitter and an electric receiver (Figure 2). The emitter located in the underwater environment generates signals, while the receiver equipped on a robot continuously measures the electric field. According to the receiver's measurements, the robot can obtain its relative position and orientation to the emitter. When there is more than one emitter, the receiver detects the frequencies of the signals to tell which emitter(s) the signals come from. Then, based on the single emitter, we construct electric-emitter architectures suitable for a large-scale environment and demonstrate three typical architectures (Figure 3).

Electric Emitter

The electric emitter located in the underwater environment consists of two copper electrodes and a circuit. To generate signals at a certain frequency, we adopt a direct digital synthesizer (DDS) in the circuit for the emitter. The DDS is a low-power, programmable waveform generator capable of producing sine, triangular, and square wave outputs. The output frequency and phase are software programmable, allowing easy tuning. In our circuit, we use three DDSs (the chip model is AD9833 from Analog Devices), each of which can generate a sinusoidal wave with a set frequency. Therefore, an emitter is able to generate single-, dual-, or three-frequency signals when one, two, or three DDSs are activated, respectively. In Figure 2, an example of the single-frequency case is shown, where two emitters generate single-frequency signals at the frequencies of f_1 and f_2, respectively.

Electric Receiver

The electric receiver on a robot is composed of four copper electrodes and a receiving circuit. To eliminate the influence of the electric potential reference on the measurements, we take the electric potential differences between each pair of electrodes as the measurements. Since the strength of the original signal measured by the receiver attenuates with the third power of the distance between the receiver and the emitter [16], it needs to be amplified and filtered.

To this end, first, the original signal is processed through a bandpass filter with a maximum gain of 100, which includes a high-pass second-order Chebyshev filter, a low-pass fourth-order Butterworth filter, a low-pass second-order Chebyshev filter, and a high-pass second-order Chebyshev filter. Figure 5 shows the amplitude–frequency response characteristics of the bandpass filter. It has a stable gain in the frequency range of 2–7 kHz and suppresses the indoor 50/60-Hz ac signal very well. Table 2 summarizes the main parameters of the

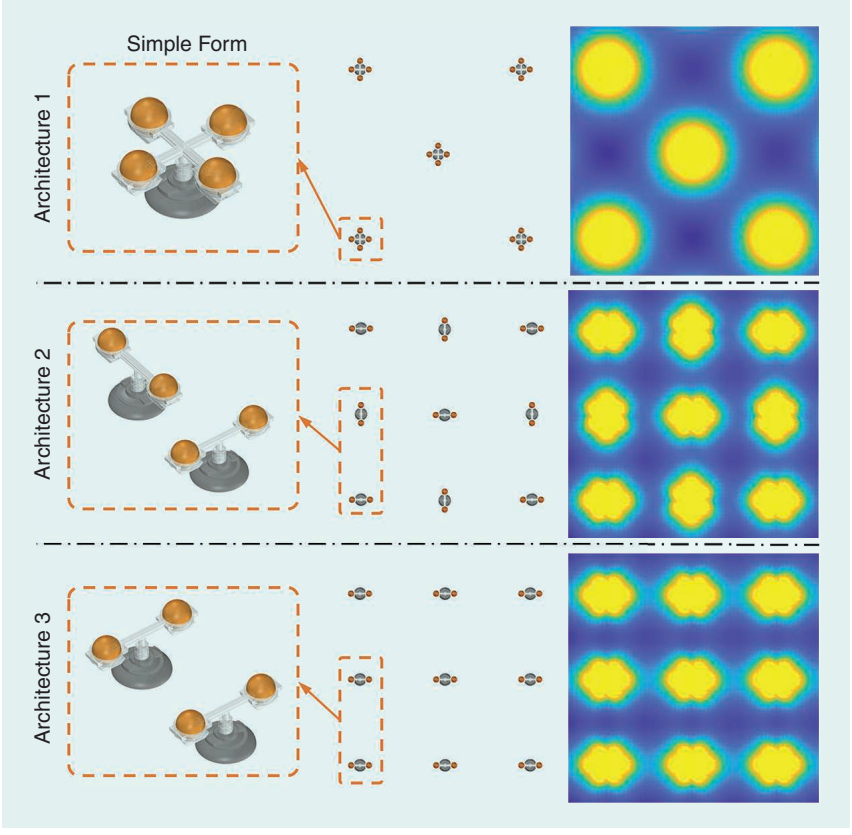

Figure 3. Three typical distributed electric-emitter architectures. Columns from left to right denote each configuration's simple form, configuration, and the schematic diagram of the distribution of electric field intensity. In the schematic diagrams, the yellow (respectively, blue) area represents the high (respectively, low) electric field intensity.

high-pass and low-pass filters. Second, considering that the signal amplitude may still not be enough to meet the needs of engineering applications, a dynamic gain with an amplification range of 1–64 times is further added based on the sampling feedback. In this way, the total amplification of the original signal is 100–6,400 times. Finally, the fast Fourier transform (FFT) technique is applied to the amplified signal to extract its amplitude and phase, which are then sent to the CPU (i.e., a Raspberry Pi) of the circuit to be further calculated to obtain the perception information.

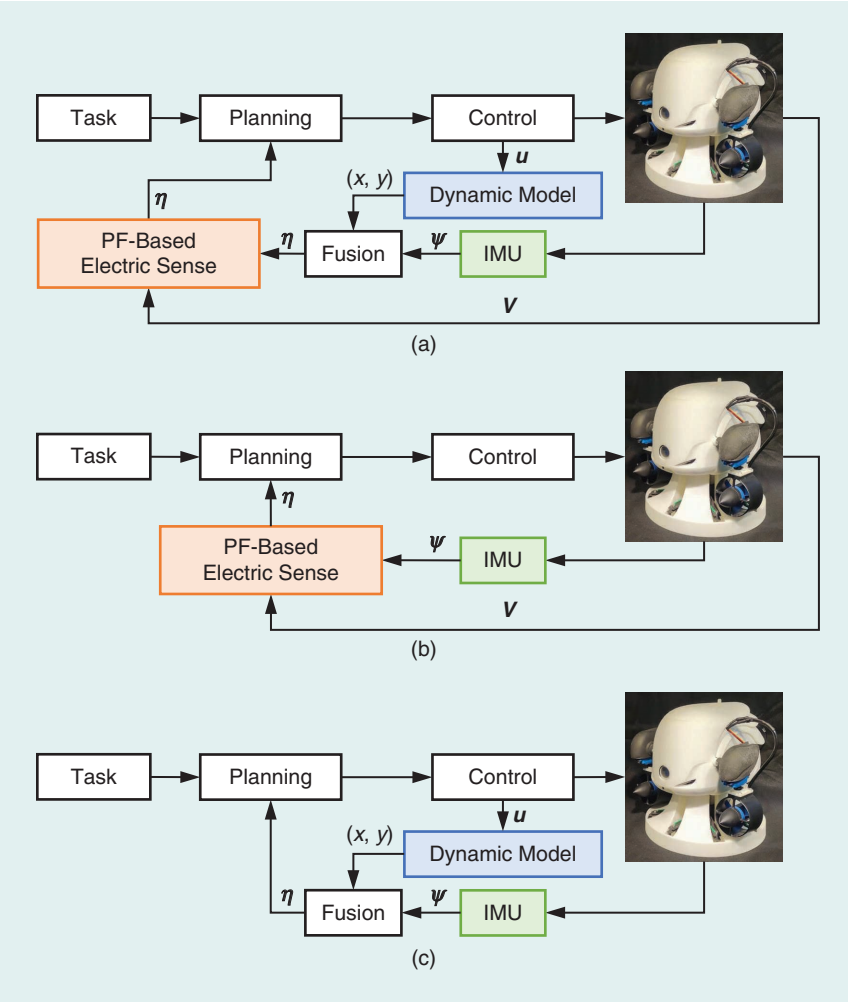

Figure 4. Three localization methods. (a) Electric sense + IMU + dynamic model, (b) electric sense + IMU, (c) IMU + dynamic model.

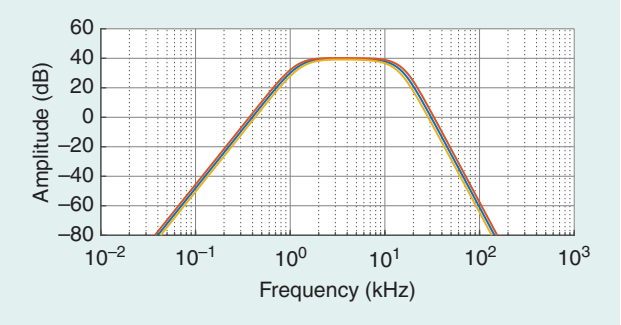

Figure 5. Amplitude–frequency response characteristics of the bandpass filter. The resistance's tolerance is 1%, and the capacitance's tolerance is 5%. The blue line is the result of the standard parameters, the red line is the upper limit, and the yellow line is the lower limit.

AC-Based Electric Sense

Now we introduce how to realize the underwater electric sense using our designed hardware solution. As we have mentioned, the electric emitter including two electrodes is placed in the underwater environment, while the electric receiver, which consists of four electrodes, is equipped on the robot. Relative to one emitter, we build a coordinate system in which we are able to describe the pose [including the position (x, y) and the orientation ψ] of the robot. When the robot moves, the four electrodes of the receiver fixed on the robot continuously measure the electric field generated by the emitter(s). Then, according to the theoretical model of the electric field (see the section "Model of the Electric Field") and the known physical parameters of the hardware, one can get the position information of the electrode from its measurement. Since the receiver has four electrodes, we get three independent measurements, $V_i, i = 1, 2, 3$, that further determine the three variables (x, y, ψ), i.e., the pose of the robot.

We also show the advantages of our ac-based solution by calculating its signal-to-noise ratio (SNR) and comparing it to that of the dc-based solution [13]. From the theoretical model of the electric field, we know that, under the same conditions, the strength of the signal measured by the receiver is identical under both ac- and

Table 2. The main parameters of the filters.

Filter	Gain	Passband	Stopband
High-pass second-order Chebyshev	10 dB	2 kHz	–40 dB@50 Hz
Low-pass fourth-order Butterworth	30 dB	10 kHz	–30 dB@40 kHz
Low-pass second-order Chebyshev	0 dB	7 kHz	–15 dB@40 kHz
High-pass second-order Chebyshev	0 dB	2 kHz	–40 dB@50 Hz

dc-based solutions. Then we just need to compare the noise of the signals. To this end, the standard deviation of the receiver's signal V_i when the robot is stationary is calculated as the signal's noise indoors in our laboratory. Then we have that the noise of the signal under the ac-based solution is about 2–10 μV, while the noise of the signal under the dc-based solution is about 1–3 mV [13]. That is, in terms of the SNR, the ac-based solution improves the dc-based solution by two to three orders of magnitude, thereby significantly improving the quality of the signal and further improving the detectable range of the emitter.

Electric-Emitter Architectures

Although our ac-based solution has successfully improved the detectable range compared with that of the dc-based solution, the detectable range of a single emitter is always limited. To enable the small underwater robots to locate in a large-scale environment, we further construct distributed electric-emitter architectures and show three typical architectures in Figure 3.

To construct such architectures, first of all, we need to decide on the configurations, including the positions and orientations of the emitters. For ease of expression, we assume that each of the three typical architectures shown in Figure 3 is distributed in a rectangular form that has M rows and N columns, i.e., MN emitters in total. Specifically, in Architecture 1, every two emitters occupy the same position in an orthogonal form, while in Architectures 2 and 3, the emitters are uniformly distributed so that the distances between each pair of adjacent emitters are equal. Besides, each pair of the adjacent emitters is orthogonal in Architecture 2, while all of the emitters are parallel in Architecture 3. It is worth emphasizing that the rectangular form of configurations we choose is just for ease of expression and comparison. In real applications, one can construct various configurations and even space them in a sparse configuration (see our discussions in the section "Real-World Applications").

Having a configuration of the emitters, it is more important to assign different frequencies to different emitters appropriately. In this way, by detecting the frequency of the signals it receives, the robot can tell which emitters the signals come from, and then it superimposes the known pose information of the corresponding emitters and obtains its own global localization information. To this end, a simple idea is to assign a unique frequency to each emitter. However, doing so would obviously waste too many frequency-band resources, especially when the architecture is large. To solve this problem, we apply the technique of multifrequency signals; that is, each emitter generates a signal whose frequency is a combination of multiple frequencies, while the frequency combinations of the emitters in the architecture are different. Obviously, with the help of the multifrequency technique, the frequency-band resources can be greatly conserved.

For our three typical architectures in Figure 3, we apply the dual-frequency technique to the MN emitters distributed in a rectangular form of M rows and N columns. For the emitter (i, j) lying in the ith row and jth column, its dual frequency $f_{i,j}$ combines the two frequencies f_i^{row} and f_j^{col}. Now, we only need $(M + N)$ different frequencies to enable the robots to distinguish the MN emitters.

Biomimetic Electric Sense-Based Localization

On the basis of our proposed hardware solution, we design localization approaches based on the biomimetic electric sense. To this end, we first build a theoretical model of the electric field generated by the electric emitter. Then, we construct three modules, including the dynamic-model module, the IMU module, and the electric sense module, each of which separately estimates the position and/or the orientation of the robot. Finally, by selectively fusing these modules, we propose three localization methods.

Model of the Electric Field

We first model the electric field generated by an emitter under the nonboundary case in a 3D environment, where the electric potential $V(\mathbf{s})$ is calculated by

$$V(\mathbf{s}) = \frac{V_0}{2\left(\frac{1}{R} - \frac{1}{d_e}\right)}\left(\frac{1}{\|\mathbf{s} - \mathbf{r}^+\|_2} - \frac{1}{\|\mathbf{s} - \mathbf{r}^-\|_2}\right), \tag{1}$$

where $\mathbf{s} = (x, y, z)$ is a position in the coordinate system attached to the emitter, V_0 is the voltage of the emitter, R is the radius of the emitter's electrode, d_e is the distance between the emitter's two electrodes, and $\mathbf{r}^+ = (x^+, 0, 0)$ and $\mathbf{r}^- = (x^-, 0, 0)$ are the positions of the positive and negative electrodes of the emitter, respectively. $\|\cdot\|_2$ denotes the Euclidean distance. Then, based on the preceding model for the nonboundary case, repeatedly using the mirror method [16], we build the theoretical model of the electric field for the six-plane boundary case corresponding to our experimental environment [i.e., the pool shown in Figure 6(b)]. For more details about the model for the six-plane boundary case, refer to [13].

According to the theoretical model of the electric field generated by an emitter, we are able to obtain the pose information (including the position and the orientation) of the robot from its receiver's three independent measurements V_i, $i = 1, 2, 3$.

Furthermore, we discuss the relationship among the physical parameters of the hardware and the receiver's measurements $V_i(\mathbf{s}_r)$, $i = 1, 2, 3$, where $\mathbf{s}_r$ is the relative pose of the receiver to the emitter in a 3D environment, and $\text{dis}(\mathbf{s}_r)$ denotes the distance from the receiver to the emitter. Specifically, one can see that the measurement $V_i(\mathbf{s}_r)$ has a positive correlation with the voltage of the emitter V_0, the radius of the emitter's electrode R, and the distance between the emitter's two electrodes d_e, respectively. In particular, when the distance d_e is five times larger than the radius R (i.e., $d_e > 5R$), the measurement $V_i(\mathbf{s}_r)$ is approximately directly proportional to V_0, R, and d_e, respectively. Also, the receiver's measurement $V_i(\mathbf{s}_r)$ has a positive correlation with the distance between the receiver's electrodes d_r, and this

correlation becomes an approximately directly proportional relationship when the receiver is far away from the emitter $[\mathrm{dis}(\mathbf{s}_r) > 5d_e]$. Moreover, it is obvious that $V_i(\mathbf{s}_r)$ has a negative correlation with $\mathrm{dis}(\mathbf{s}_r)$.

Perception Modules

For a robot equipped with our electric sense-based hardware as well as an IMU sensor, we construct three perception modules, including the dynamic-model module, the IMU module, and the electric sense module (Figure 4). These three modules separately estimate the position and/or orientation of the robot, which provides a basis for us to design localization methods. Here we assume that the robot swims in two dimensions because our experimental pool is not deep enough. Thus, the three perception modules focus on the perception in a 2D environment. It is worth emphasizing that our proposed electric sense hardware solution is able to work in a 3D environment (see our discussions in the section "Real-World Applications").

Dynamic-Model Module (the Blue Module in Figure 4)

This module updates the position estimation $[x_{k+1}, y_{k+1}]$ based on the previous estimation $\boldsymbol{\eta}_k$ and the control input $\mathbf{u}_k$:

$$[x_{k+1}, y_{k+1}]^T = \mathbf{Dynamic}(\boldsymbol{\eta}_k, \mathbf{u}_k), \tag{2}$$

where $\boldsymbol{\eta}_k = [x_k\ y_k\ \psi_k]^T \cdot \mathbf{Dynamic}(\cdot)$ represents the robot's dynamic model composed of a series of equations.

IMU Module (the Green Module in Figure 4)

Since the IMU sensor has very high accuracy in the short term, the IMU module updates the orientation estimation ψ_{k+1} based on the previous estimation ψ_k and the IMU data $\Delta\psi_k^{\mathrm{IMU}}$:

$$\psi_{k+1} = \psi_k + \Delta\psi_k^{\mathrm{IMU}}, \tag{3}$$

where $\Delta\psi_k^{\mathrm{IMU}}$ is the increment of the yaw angle of the IMU.

Electric Sense Module (the Red Module in Figure 4)

This module is based on the PF to fuse the estimation information, where the sampling importance resampling (SIR) algorithm [17] is adopted. Using the SIR algorithm, the electric sense module updates the pose estimation $\boldsymbol{\eta}_{k+1}$ by fusing the electric receiver's measurements $\mathbf{V} = [V_1\ V_2\ V_3]^T$ together with the estimation output from its previous module(s), i.e., the dynamic-model module and/or the IMU module. Specifically, first, for each particle i, denoted by the superscript $^{(i)}$, the pose estimation $\boldsymbol{\eta}_{k+1}^{(i)}$ is updated by adding a random noise $\epsilon_k^{(i)}$, which represents

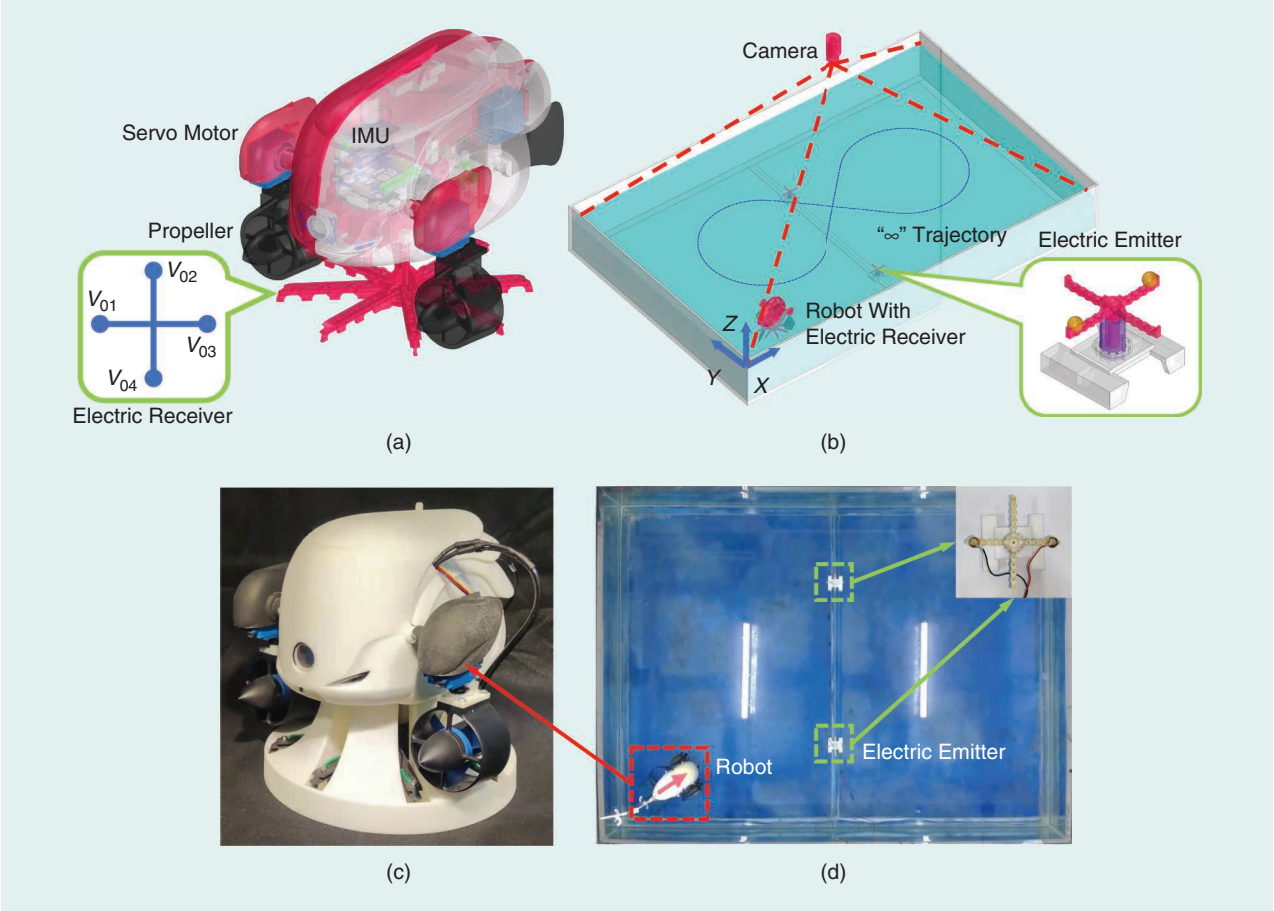

Figure 6. Small underwater robot and experimental platform. The electric receiver is equipped on the robot, while the electric emitters are located in the pool.

the external disturbance, the measurement errors, and so on. Then, we sequentially update the particle importance weight $w_k^{(i)}$. Third, we normalize the importance weights of all of the particles and calculate the final value of the pose estimation. That is,

$$\begin{aligned}\boldsymbol{\eta}_{k+1}^{(i)} &= \boldsymbol{\eta}_{k+1} + \epsilon_k^{(i)},\\ w_{k+1}^{(i)} &= p(\mathbf{V}_{k+1} \mid \boldsymbol{\eta}_{k+1}^{(i)}) w_k^{(i)},\\ \boldsymbol{\eta}_{k+1} &= \sum_{i=0}^{N-1} \boldsymbol{\eta}_{k+1}^{(i)} \frac{w_{k+1}^{(i)}}{\sum_{i=0}^{N-1} w_{k+1}^{(i)}},\end{aligned} \tag{4}$$

where $p(\mathbf{V} \mid \boldsymbol{\eta}^{(i)}) = e^{\|\mathbf{V}-\mathbf{V}(\boldsymbol{\eta}^{(i)})\|_2^2 / V_{\text{std}}^2}$ is the importance weight of the measurements, and V_{std} is the factor of the importance weight.

We would like to mention that, according to the principle of the electric sense, our proposed electric sense-based scheme can provide not only the position (x, y) but also the orientation ψ of the robot. However, specific to the electric sense module, the robot's position is updated using the electric sense, while the robot's orientation information is mainly contributed from the IMU module, where the electric sense just serves as an auxiliary. The reason is that the IMU sensor is a very cheap and established way to estimate the orientation. Thus, we focus on estimating the position of the robot based on the electric sense when designing the localization algorithm of the electric sense module.

Multi-Information Fusion-Based Localization Methods

By selectively fusing the previous three perception modules, we propose three localization methods (Figure 4): 1) electric sense + IMU + dynamic model, 2) electric sense + IMU, and 3) IMU + dynamic model.

Specifically, the IMU module is chosen as a necessary part of all three localization methods. Since the emitters are fixed in the underwater environment, their orientations are known ahead of time by the robot. Thus, the IMU on the robot can be calibrated before the localization starts, so that the robot obtains a more accurate initial orientation. Then, for the dynamic-model module and the electric sense module, we choose one or both of them to integrate with the IMU module. These designs enable us to evaluate the contributing factors of the electric sense-based localization.

Our Robot and Experimental Platform

To verify and evaluate our proposed hardware solution to the electric sense and the corresponding localization methods, we design a robot equipped with an electric receiver for conducting the experiments. Thus, in this section, we first introduce the robot's design and its dynamic model and then present the experimental platform including the physical parameters of the electric sense hardware.

Design of the Robot

The small underwater robot that we have developed is shown in Figure 6(a) and (c); its size is about 34 × 27 × 24 cm^3 (length × width × height). The robot has two propellers and a caudal fin. Each propeller is steered by a servo motor so that the direction of propulsion can be flexibly changed. The caudal fin is designed to increase the steering resistance of the robot, allowing it to swim straighter, so it is fixed on the robot. Moreover, an electric receiver consisting of four electrodes is equipped on the bottom of the robot to realize electric sense. For our experiments in this article, we only need the robot to swim in two dimensions because of the limitation of the experimental pool, so we just change the thrust of the two propellers but fix their thrust directions.

The Dynamic Model

Based on the design of the robot as well as its previous specific actuation mode when used in our experiments, we construct a 2D dynamic model of the robot. Following the notation developed by Fossen [18], the dynamic model of an underwater robot is generally described by the equation

$$\mathbf{M}\dot{\mathbf{v}} + \mathbf{C}(\mathbf{v})\mathbf{v} + \mathbf{D}(\mathbf{v})\mathbf{v} = \boldsymbol{\tau}, \tag{5}$$

where $\mathbf{v}$ denotes the vehicle velocity in the body-fixed frame, which contains the vehicle surge velocity, sway velocity, and yaw velocity. $\mathbf{M}$ is the added mass and inertia matrix. $\mathbf{C}(\mathbf{v}) \in \mathbb{R}^{3\times 3}$ is the matrix of Coriolis and centripetal terms. $\mathbf{D}(\mathbf{v})$ is the drag matrix. The propulsion forces and moments $\boldsymbol{\tau} \in \mathbb{R}^{3\times 1}$ constitute the vector of body-frame forces, which can be written as

$$\boldsymbol{\tau} = \mathbf{B}\mathbf{F} = \begin{bmatrix} 1 & 0 \\ 0 & 1 \\ \frac{a}{2} & -\frac{a}{2} \end{bmatrix} \begin{bmatrix} f_1(u_1) \\ f_2(u_2) \end{bmatrix}, \tag{6}$$

where a is the distance between the robot's two propellers, and $u_1, u_2 \in [0, 1]$ are the normalized control outputs of the left and right propellers, respectively. $f_1(\cdot), f_2(\cdot)$ are the mapping relationships between the control input u and the thrust vector $\mathbf{F}$, and $\mathbf{F}$ to $\boldsymbol{\tau}$ is a linear mapping.

Based on the robot's dynamic model, we use the model predictive control (MPC) method as the control law for the free-swimming robot. Specifically, we establish a rolling optimization model and perform continuous convex optimization [19]. We would like to emphasize that the control law will not affect the performance of our electric sense.

The Experimental Platform

As shown in Figure 6(b), we conduct the experiments in a pool of size 3 × 2 × 0.38 m^3 (length × width × height). There is an overhead camera to capture the position and orientation of the robot, which is used as the ground truth of our localization experiments.

For the electric sense-based hardware used in our experiments, the physical parameters of the emitters and the receiver are as follows: the emitter's voltage V_0 is 5 V, the radius of the emitter's electrode R is 0.75 cm, the distance between the emitter's two electrodes d_e is 10 cm, and the distance between the receiver's two electrodes d_r is 20 cm.

Furthermore, to evaluate the three typical emitter architectures, considering the limiting size of the pool, we use the simple forms of their configurations, as shown in Figure 3 (left column). Specifically, each of the three architectures contains two emitters. The position and orientation of emitter 1 for all three architectures are (1.5 m, 0.5 m, 0°). The position and orientation of emitter 2 are (1.5 m, 0.5 m, 90°), (1.5 m, 1.5 m, 90°), and (1.5 m, 1.5 m, 0°), for Architecture 1, Architecture 2, and Architecture 3, respectively.

Localization Experiments

Now we conduct the localization experiments for the small underwater robot in four scenarios to fully demonstrate the effectiveness of our proposed hardware solution and localization methods. Specifically, in the first two scenarios, we separately conduct localization experiments for a stationary robot (Experiment 1) and a robot under towing (Experiment 2); that is the robot is set to be without self-motion (its control output $\mathbf{u} = \mathbf{0}$). Then, in the last two scenarios, we conduct localization experiments for an autonomous swimming robot ($\mathbf{u} \neq \mathbf{0}$), including the position tracking problem (Experiment 3) and the kidnapped robot problem, which is much more complicated (Experiment 4).

Experiment 1: Stationary Robot

In this scenario, we fix the pose of the robot and then test our electric sense-based localization scheme. Since the dynamic model of the robot does not work ($\mathbf{u} = \mathbf{0}$), the "electric sense + IMU + dynamic-model" method is equivalent to the "electric sense + IMU" method, and the "IMU + dynamic-model" method is invalid. Therefore, in this scenario, we only need to verify the localization ability of the "electric sense + IMU" method. Note that this is a global localization problem since the robot's initial position is unknown to the robot. To this end, the initial positions of the particles, which are used in the SIR algorithm in the electric sense module, are randomly distributed throughout the experimental pool; that is, $x^{(i)} \in [0, 3]$ m and $y^{(i)} \in [0, 2]$ m. Meanwhile, the angle of the IMU equipped on the robot is calibrated according to the coordinate system before the experiment starts, thereby giving a rough actual value as the initial orientation of the robot. As shown in Figure 7(a), the robot is fixed at nine poses [x(m), y(m), ψ(°)] of [0.5, 0.4, 0], [0.5, 0.4, 45], [0.5, 0.4, 90], [2.6, 1.6, 180], [2.6,1.6, 225], [2.6, 1.6, 270], [2.0, 0.5, 270], [2.0, 0.5, 135], and [2.0, 0.5, 0], respectively. The robot's actual pose is recognized by the overhead camera as the ground truth. The position error is defined by the Euclidean distance between the position estimation and the ground truth, and the orientation error is defined by the difference between the orientation estimation and the ground truth. The experiments under each pose are repeated three times. The experimental results are shown in Figure 7.

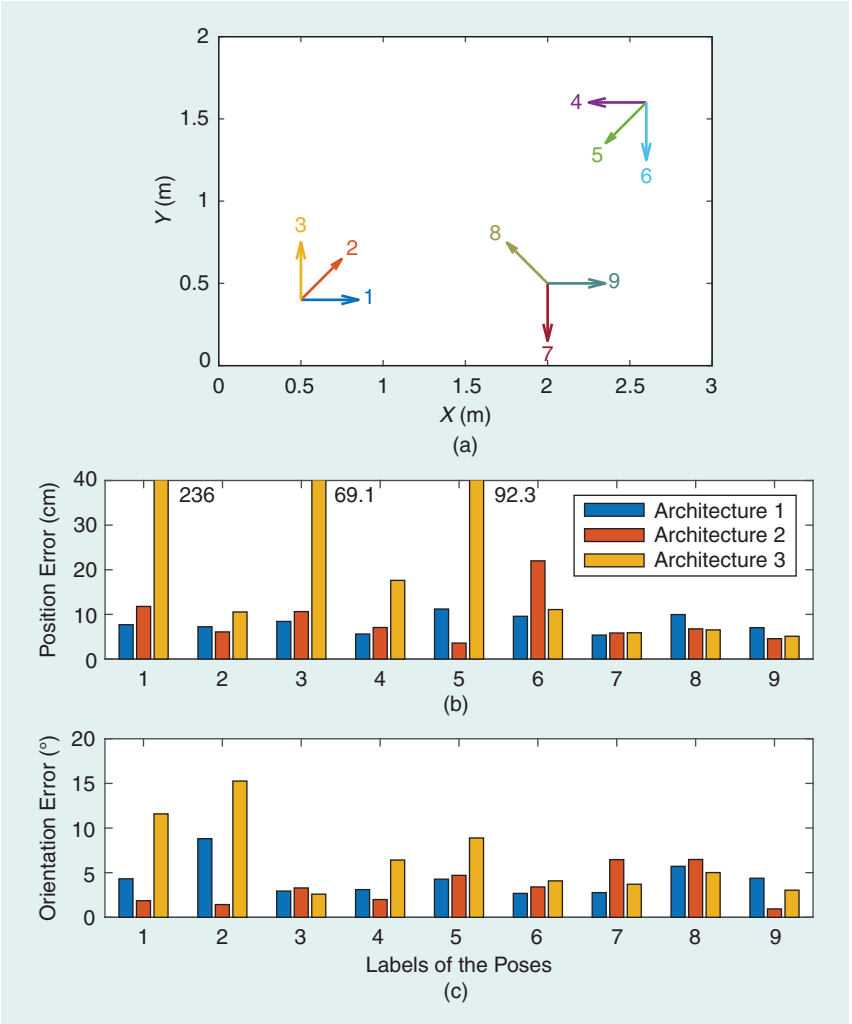

Figure 7. Experiment 1: Localization of a stationary robot under the "electric sense + IMU" method. (a) The robot's nine poses, where the arrow direction represents the robot's orientation and the start of the arrow corresponds to the robot's position. (b) The average position errors for the nine poses under each emitter architecture. For Architecture 3, three of the average position errors (for poses 1, 3, and 5) are out of range of the figure. (c) The average orientation errors for the nine poses under each architecture. Archi.: Architecture.

As shown in Figure 7(b) and (c), one can see that the position errors and the orientation errors under Architecture 3 are worse than those under Architectures 1 and 2. Specifically, in terms of the position estimation, there are failures under Architecture 3 for three poses (poses 1, 3, and 5). The errors of Architecture 1 and the errors of Architecture 2 are on

the whole equivalent. Comparing the emitters' poses among the three architectures, one can conclude that the architectures with orthogonal emitters (Architectures 1 and 2) perform better in this static localization scenario.

Experiment 2: Robot Under Towing

Unlike the stationary state used in Experiment 1, in this scenario, we pull the robot from one position to another with a rope to verify the electric sense-based localization method under passive motion, as shown in Figure 8 (left column). While similar to Experiment 1, the localization task in this scenario is also a global localization problem, and we only need to verify the "electric sense + IMU" method. The robot's pose is separately estimated under the three architectures, and the experiments under each architecture are repeated three times. The experimental results are shown in Figure 8.

As shown in Figure 8, one can see that Architecture 1 has the fastest convergence speed, Architecture 2 is the second fastest, and Architecture 3 is the slowest. Further, we calculate the average position errors and the orientation errors under the electric sense-based localization method during the time period 10–30 s. The average position errors under the three architectures are 6.0 cm, 7.9 cm, and 11.4 cm, respectively. Meanwhile, the average orientation errors under the three architectures are 7.0°, 6.7°, and 6.8°, respectively. Thus, we can also draw conclusions similar to those of Experiment 1 that, in the towing scenario, the architectures with orthogonal emitters (Architectures 1 and 2) perform better. Besides, the initial position errors are quite different for each experiment since the initial positions of all particles are randomly generated, and the algorithm converges very fast in the first iteration.

Experiment 3: Position Tracking of Autonomous Swimming Robot

Unlike the passive motion in Experiment 2, in this localization scenario, the robot is steered by the MPC law to follow a "∞"-shaped path. We verify the three localization methods in this scenario. The robot equipped with the receiver starts from the position $[0.5, 0.4]$ m for each run. The experimental results are shown in Figure 9, and their statistical results are summarized in Table 3.

As shown in Figure 9, one can see that the position errors under the "electric sense + IMU + dynamic-model" method keep a good boundary, making it clearly superior to the other methods and appropriate for long-term localization. It is further shown that the electric sense module plays an important role, compared with the drifts under the "IMU + dynamic-model" method. On the other hand, together with the unstable errors under the "electric sense + IMU" method, one can conclude that the dynamic-model module plays a key role. In addition, together with the results in Table 3, we can draw two more conclusions. First, under the "electric sense + IMU + dynamic-model" method, there is no significant difference in the results of the three architectures. Second, Architecture 3 is not necessarily inferior to Architectures 1 and 2 in this autonomous swimming scenario.

Experiment 4: Kidnapped Robot Problem

For mobile robot localization, the kidnapped robot problem refers to a situation in which the robot is instantly moved to another position without being told. Although such a scenario rarely happens in practice, it is often used to test the ability of the localization method to recover from failures [20]. In the position tracking problem (Experiment 3), the initial position is roughly true. However, the initial position is wrong in the kidnapped robot problem. Thus, the kidnapped robot problem is more difficult than the global localization problem. In the experiment, the robot is first given a wrong initial estimation, and then we evaluate whether the robot can recover from the failure. The errors of the initial position are [0.4, 0.2] m, [–0.4, –0.2] m, [–0.6, –0.3] m, [0.6, 0.3] m, and [0.5, 0.5] m, respectively. The errors of the initial orientation are 0°, −20°, 0°, −20°, and −20°, respectively. Besides, we choose Architecture 2 and the above-mentioned "∞"-path. The experimental results are shown in Figure 10, and their statistical results are summarized in Table 4.

From Figure 10, one can see that the position errors of the "electric sense + IMU + dynamic-model" method converge faster. Specifically, the position errors of the "electric sense + IMU + dynamic-model" method converge to within 5 cm in the first 20 s, and the position errors of the "IMU + dynamic-model" method drift. Our "electric sense + IMU + dynamic-model" method has a good performance in this scenario. Similarly, we can also see from Table 4 that the average errors of the "electric sense + IMU + dynamic-model" method are better than those of the "IMU + dynamic-model" method. In conclusion, the "electric sense + IMU + dynamic-model" method under Architecture 2 is effective in this very complicated scenario, i.e., the kidnapped robot problem.

Discussion

To gain insight into the effectiveness of our proposed electric sense-based scheme, in this section, we first evaluate the detectable range of a single emitter and propose measures to increase the detectable range. Then we discuss what contributes to the performance differences among different electric-emitter architectures. Further, we present the possible extensions of our scheme to real-world applications.

Detectable Range

As a sensing technology, the working scope of our electric sense-based scheme is one of the key properties. Therefore, we evaluate the detectable range of the electric emitter and then discuss how to increase the detectable range.

It is known that the detectable range is directly related to the strength of the signal measured by the receiver as well as the noise at the receiver. As introduced in the section "Model of the Electric Field," the theoretical model of the electric field gives the relationship between the receiver's measurements $V_i(\mathbf{s}_r), i = 1, 2, 3$ and the receiver's relative pose $\mathbf{s}_r$ to the emitter as well as other physical parameters of the electric sense

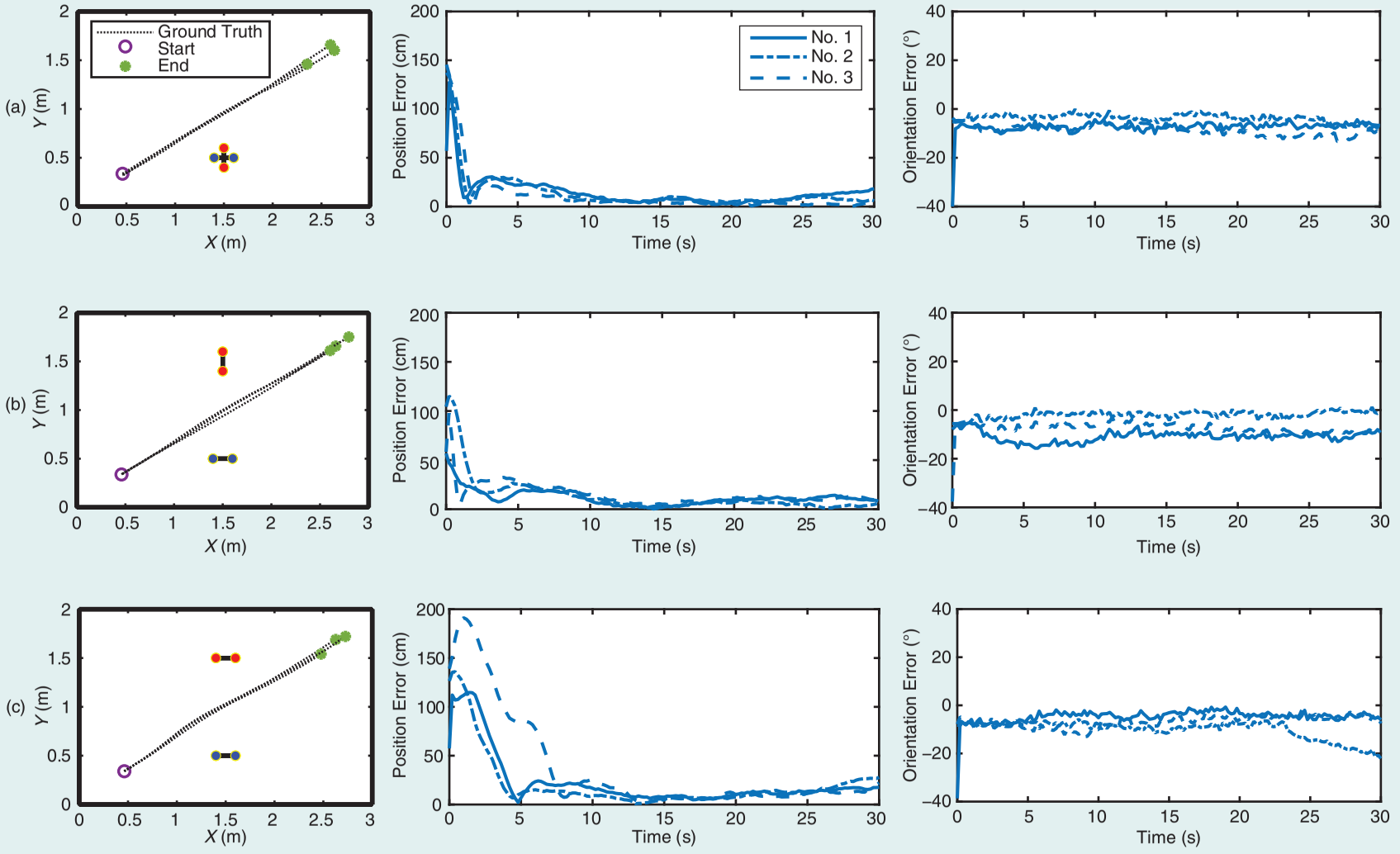

Figure 8. Experiment 2: Localization of a robot under towing under the "electric sense + IMU" method. From top to bottom: (a) Architecture 1, (b) Architecture 2, (c) Architecture 3. (Left column) The robot's trajectories of ground truth (black dotted lines), emitter 1 (blue circles), and emitter 2 (red circles). (Middle column) The position errors compared to the ground truth. The different lines represent repeated experiments. (Right column) The orientation errors compared to the ground truth.

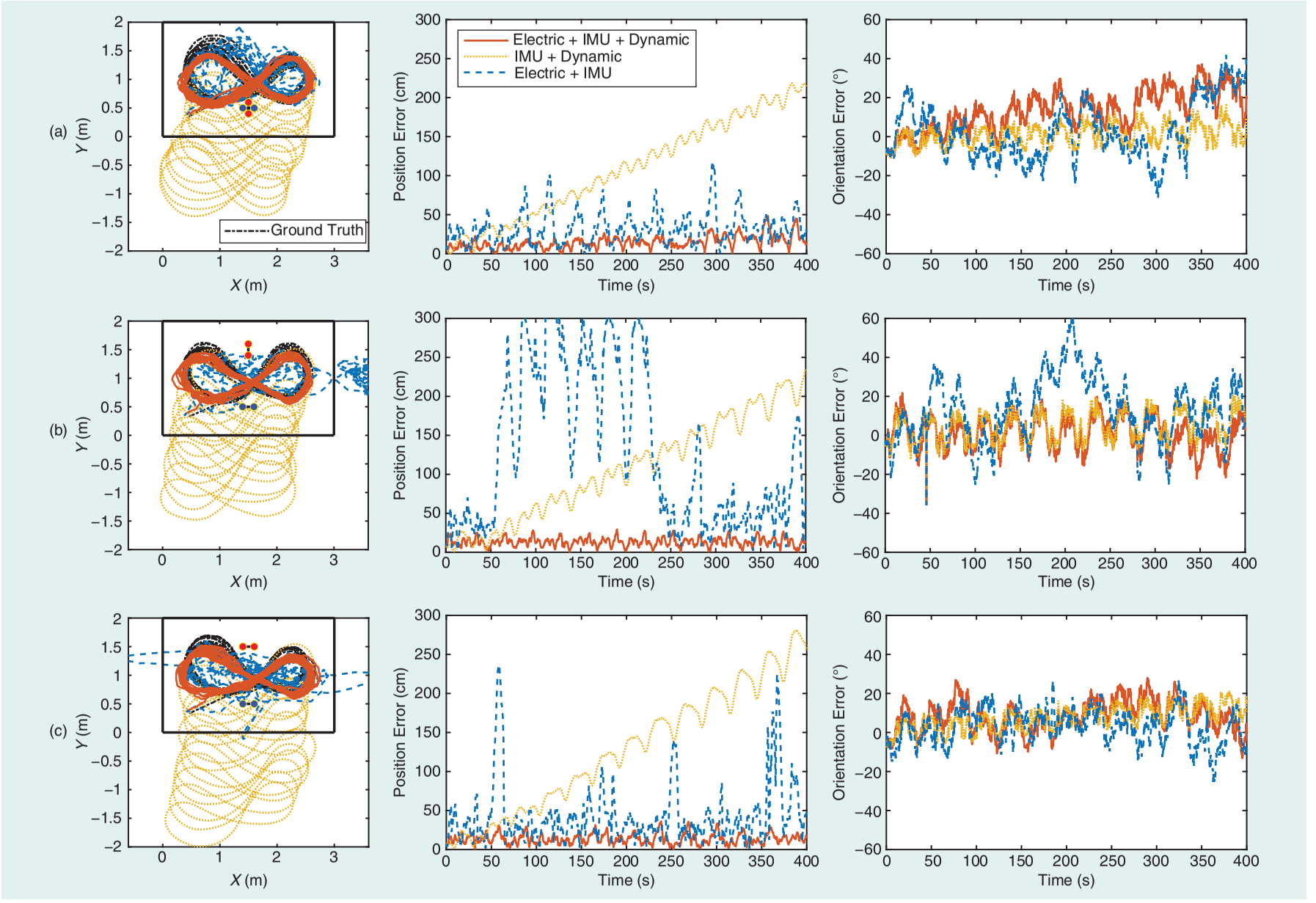

Figure 9. Experiment 3: Position tracking of a free-swimming robot under our three localization methods. From top to bottom: (a) Architecture 1, (b) Architecture 2, (c) Architecture 3. (Left column) The robot's trajectories of the ground truth (black dotted lines), the estimated trajectories under the "electric sense + IMU + dynamic-model" method (red lines), the "electric sense + IMU" method (blue lines), and the "IMU + dynamic-model" method (yellow lines). (Middle column) The position errors compared to the ground truth. (Right column) The orientation errors compared to the ground truth.

hardware. Then, we consider the noise at the receiver. Since our proposed electric sense-based scheme can be applied to different underwater robots or vehicles, the noise we focused on refers to the environmental noise at the receiver, excluding the electrical noise from robotic components, such as propellers. When working indoors, the noise in different rooms varies greatly because the environmental noise mainly comes from the noise of electrical appliances and experimental equipment. However, when working in the wild, interference factors, such as electrical appliances are reduced; thus, the environmental noise is always much smaller than that indoors. Therefore, we believe that our following evaluation of the detectable range is relatively conservative since our experiments are conducted indoors in the laboratory and are inevitably affected by various indoor appliances.

Now we are ready to evaluate the detectable range of a single emitter by calculating the voltage of the receiver and its SNR level. Specifically, for the electric sense-based hardware used in our experiments, taking its physical parameters given in the section "The Experimental Platform," the receiver's

Table 3. The experimental results of Experiment 3.

Method	Emitter	err_{pos} (cm)	err_{ori}
Electric + IMU + Dynamic	Archi. 1	16.6	14.8°
	Archi. 2	15.5	**10°**
	Archi. 3	**15.3**	10.3°
Electric + IMU	Archi. 1	**35.5**	14.3°
	Archi. 2	132	17.9°
	Archi. 3	44.7	**7.2°**
IMU + Dynamic	Archi. 1	114.4	**6.8°**
	Archi. 2	**113.7**	10.3°
	Archi. 3	135	9.3°

Archi. Architecture; err_{pos} (respectively, err_{ori}) is the average position error (respectively, orientation error) under the three localization methods.

Table 4. Experimental results of Experiment 4.

	Electric + IMU + Dynamic		IMU + Dynamic	
Initial error	err_{pos} (cm)	err_{ori}	err_{pos} (cm)	err_{ori}
[0.4 m, 0.2 m, 0°]	**13.2**	9.1°	38.5	**7°**
[–0.4 m, –0.2 m, –20°]	**16.4**	**7.6°**	76.3	12.3°
[–0.6 m, –0.3 m, 0°]	**19.2**	7.2°	78.9	**4.4°**
[0.6 m, 0.3 m, –20°]	**15.4**	**7.6°**	63.9	12.7°
[0.5 m, 0.5 m, –20°]	**16.3**	**7.4°**	60.8	13.5°

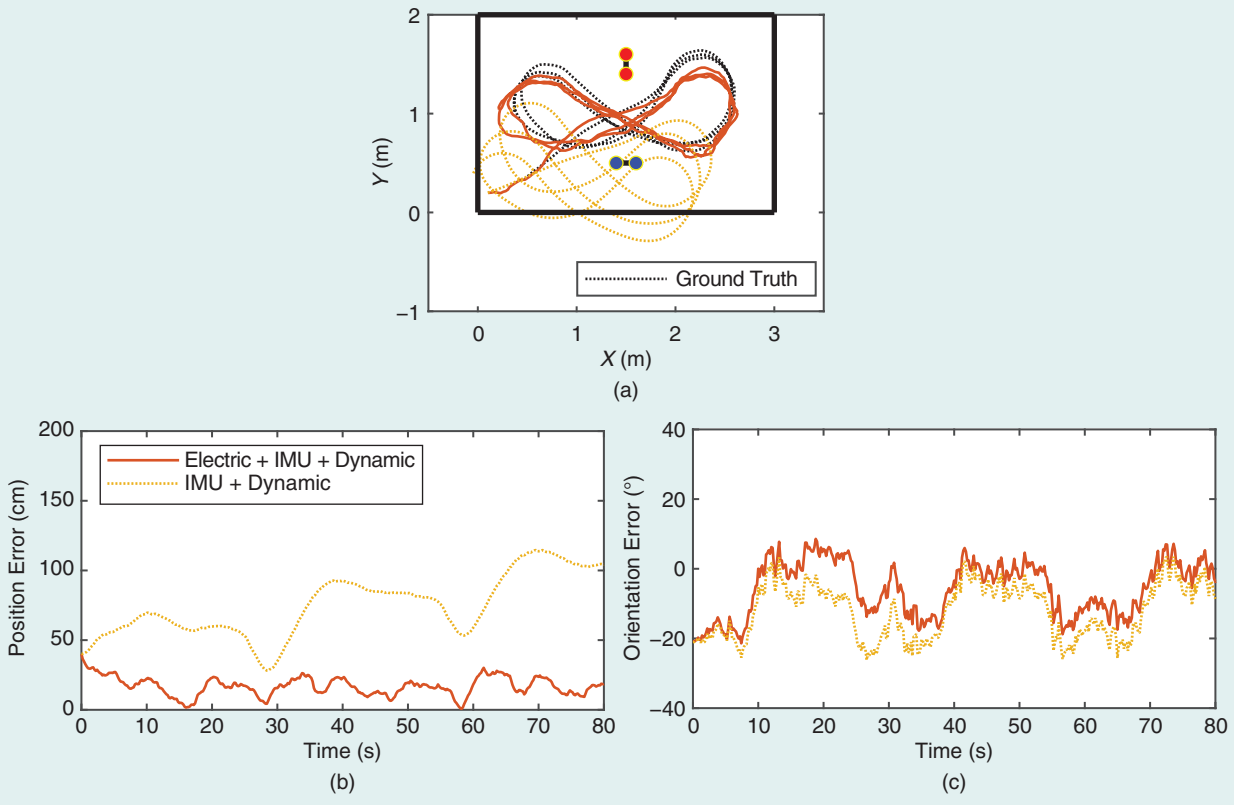

Figure 10. Experiment 4: Kidnapped robot problem of a free-swimming robot under two localization methods. The errors of the initial pose are about [–0.4 m, –0.2 m, –20°]. (a) The robot's trajectories of the ground truth (black dotted lines), the estimated trajectories under the "electric sense + IMU + dynamic-model" method (red lines), and the "IMU + dynamic-model" method (yellow lines). (b) The position errors compared to the ground truth. (c) The orientation errors compared to the ground truth.

measurements $V_i(\mathbf{s}_r)$ are calculated by the theoretical model of the electric field. Then we calculate the SNR ($:= 20\log_{10} V_{\text{rms}}/V_{\text{noise}}$) of the receiver's signal V_i, where V_{rms} is the root mean square of the receiver's voltage on the quadrature method, and the signal's noise V_{noise} is denoted as the standard deviation of the receiver's signal V_i when the robot is stationary. Thus, the signal's noise is about 2–10 μV, whose median is 5 μV.

Taking these previous calculations, we can obtain the receiver's measurements V_i and its SNR at every pose $\mathbf{s}_r$ of the receiver relative to the emitter. Since $V_i(\mathbf{s}_r)$ has a negative correlation with the distance $\text{dis}(\mathbf{s}_r)$ from the receiver to the emitter, one can check that, for a given voltage threshold V_{thr}, the set of positions at which $V_{\text{rms}} \geq V_{\text{thr}}$ will form a region whose boundary line (also called the *equipotential line*) consists of the positions at which $V_{\text{rms}} = V_{\text{thr}}$. To provide an intuitive demonstration, we select four pairs of the typical voltage threshold V_{thr} and its SNR as (0.5 mV, 40 dB), (0.25 mV, 34 dB), (0.1 mV, 26 dB), and (0.05 mV, 20 dB) and draw the corresponding boundary lines in Figure 11. It is shown that each boundary line is an approximate ellipse. The extreme values of the distances from the emitter's center to each boundary line are denoted as D_{min} and D_{max}, and their values are also shown in Figure 11. That is, if it is required that the receiver's signal is valid when its SNR exceeds 20 dB, the emitter's maximum detectable range is around 2.32–2.76 m. Actually, we have conducted testing experiments and found that the receiver's signal with an SNR of 20 dB is enough for localization.

To sum up, for the electric sense-based hardware with the physical parameters of $V_0 = 5$ V, $R = 0.75$ cm, $d_e = 10$ cm, and $d_r = 20$ cm, its emitters' maximum detectable range is around 2.32–2.76 m. Until now, we have evaluated the detectable range of a single emitter. We believe that the detectable range is not small compared with the physical parameters of the hardware.

Moreover, we discuss how to increase the detectable range. From the theoretical model of the electric field, one can see that the receiver's measurement V_i has a positive correlation with four physical parameters separately, including the voltage of the emitter V_0, the radius of the emitter's electrode R, the distance between the emitter's two electrodes d_e, and the distance between the receiver's electrodes d_r. Considering that high voltages could pose a variety of risks (e.g., to aquatic animals), we can increase the receiver's measurement and thus improve the detectable range by easily increasing one or more of the other three physical parameters, R, d_e, and d_r.

Electric-Emitter Architectures

Now we gain insight into what contributes to the performance differences among the three typical electric-emitter architectures, Architecture 1, Architecture 2, and Architecture 3. First of all, we mention that the emitter density of the three architectures is identical, and each emitter has the same physical parameters (i.e., the voltage of the emitter V_0, the radius of the emitter's electrode R, and the distance between the emitter's two electrodes d_e). Therefore, a comparison of the three architectures is essentially a comparison of the uniformity of the distribution of the electric field, including the uniformity of the intensity and the uniformity of the direction.

Ideally, our expectation is that the electric field intensity is equal everywhere in space, so that the localization accuracy of the robot in different spatial positions will be relatively constant. However, the emitter's physical properties have already determined the nonuniformity of its generated physical field (i.e., electric field intensity), as shown in Figure 11. Meanwhile, the architecture of the emitters, including both the position and the orientation of each emitter, will further affect the uniformity of the electric field intensity. Therefore, our expectation becomes making the area above a certain voltage threshold as large as possible (e.g., the yellow area in Figure 3). On the other hand, the uniformity of the electric field direction is affected by the orientation of each emitter in the architecture. If a robot can obtain a certain strength of the signal in more orientations, the robustness of its localization will be increased compared with the case when the signal is obtained in only one orientation.

Following the previous discussions, using the theoretical model of the electric field, we calculate the spatial distribution

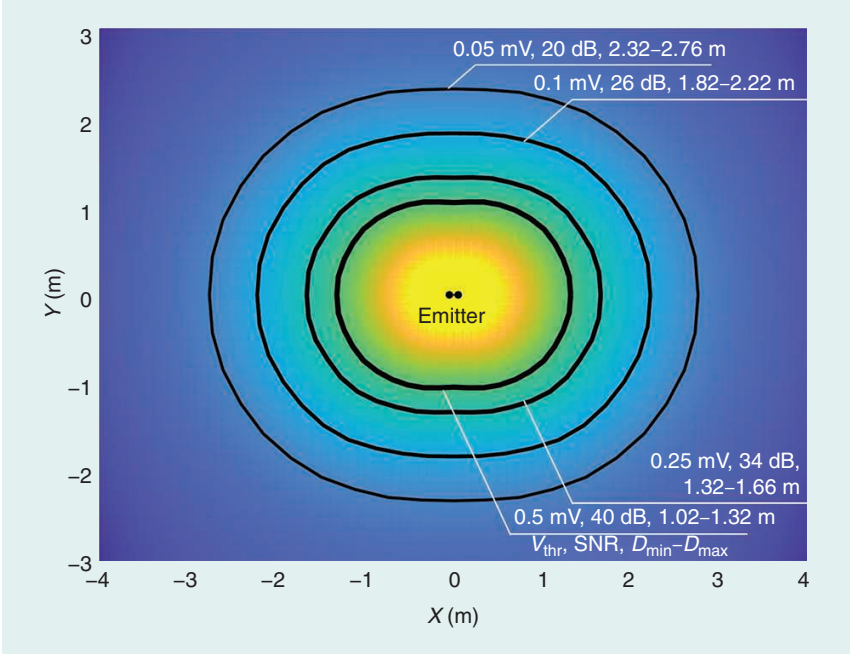

Figure 11. A schematic diagram of the distribution of electric field intensity for a single emitter. The yellow (respectively, blue) area represents the high (respectively, low) electric field intensity. The black lines denote the equipotential lines under the different voltage thresholds V_{thr} and the corresponding SNR.

of the electric field intensity for the three architectures separately, as shown in the right column of Figure 3. When such architectures are used in a specific localization task for the robot, their performance can be analyzed according to the uniformity of the distribution of the electric field, as we have discussed previously.

Specific to the localization tasks in the section "Localization Experiments," we talk a little more about the performance of the three architectures. In the static scenario, the localization may fail since the information obtained by the electric receiver is partial and limited, which is very obvious in Architecture 3. On the other hand, in the towing scenario, the localization can be successful since the robot is continuously acquiring new electric measurements. The experimental results under Architecture 3 also reflect this. The towing scenario can be equivalent to the displacement caused by the external flow or the external force. This means that our biomimetic electric sense-based localization method can be applied to an unknown flow environment, which is very meaningful for practical applications. Besides, the two types of scenarios without self-motion reflect that Architecture 3 may be a poor architecture, while Architectures 1 and 2 perform better. This phenomenon implies that the localization results are better when adjacent emitters are orthogonal.

The previous discussion may provide a guide for us to construct electric-emitter architectures for different working tasks.

Real-World Applications

Based on the previous evaluations and discussions, we now try to conclude the appropriate real-world application environments for our proposed electric sense-based scheme. First, the hardware of our scheme can be customized for different sizes of the robots/vehicles or for different scales of working spaces since the detectable range of a single emitter can be easily and flexibly changed by adjusting the physical parameters of the emitter, such as the distance between its two electrodes.

Second, our localization scheme can be used in a large-scale 2D (respectively, 3D) environment by deploying a 2D (respectively, 3D) emitter architecture, especially considering the good property that the architecture is allowed to be built in a sparse manner. Specifically, we now discuss the issue of emitter density. On one hand, according to our previous evaluation of the maximum detectable range (2.32–2.76 m) of a single emitter, the emitters can be placed at intervals of about 4.64–5.52 m to make sure the robots realize a continuous real-time localization. On the other hand, if a lower emitter density is still needed, the emitters can also be placed sparsely (e.g., at intervals larger than 5.52 m and even up to 10–20 m) since the convergence of our localization method in such a sparse situation has been verified by Experiment 4 (the kidnapped robot problem). Once the robot is within the detectable range of the emitters, the estimation can converge quickly, so the robot doesn't need to always stay in the detectable range. We want to claim that, although our evaluations of the maximum detectable range and further the densities of the emitter array are all in a 2D environment, it is similar to the situation in a 3D environment since the electric field generated by the emitter is 3D. Note also that the emitter densities are evaluated based on the maximum detectable range, which is determined by the physical parameters of the hardware used in our experiments, and the maximum detectable range can easily be increased by adjusting these parameters and thus further decreasing the density of the emitter array.

Third, by integrating other sensors (e.g., the pressure sensors and the IMU sensors), which are also low in cost, the working scope of our localization scheme could be further improved at low cost. Concretely, one can equip the robot with a pressure sensor (e.g., CPS131 from Consensic, Inc. or MS5803-01BA from TE Connectivity Ltd., used frequently in our previous robots [21]). The pressure sensor can obtain the ground truth of the robot's depth by calibrating the current atmospheric pressure, which may be more reliable than using an extra camera to calculate the depth. Based on the pressure sensor, the change in depth can be obtained at millimeter-level accuracy. Besides, the robot's pitch and roll can be obtained through the IMU. When the robot works in the coverage of the 2D or 3D emitter architecture, the pressure sensor and the IMU are integrated with the electric sense for perception and localization. When the robot is out of the coverage of the emitter architecture, the pressure sensor and the IMU keep working. Once the robot is back within the architecture's coverage, the electric sense works, and the estimation will be corrected quickly.

In summary, although the experiments conducted in this article are in a 2D setting, and the experimental pool is not large, our proposed electric sense-based scheme is easily extended for large-scale 3D working environments. We also mention that, as far as the authors are aware, few studies have considered the electric sense for free-swimming robots even in two dimensions.

Conclusion and Future Work

In this article, for free-swimming small underwater robots in a large-scale environment, we propose a novel electric sense-based localization scheme, including a hardware solution and three model-based perception methods. First, our hardware solution is composed of an ac-based electric receiver furnished on the robot and ac-based electric emitters fixed on the seabed. The robot uses the measurements of its receiver to estimate its relative position and orientation to the emitters on the seabed. Second, we construct distributed electric-emitter architectures to enable localization in a large-scale environment. Third, we design three localization methods by selectively fusing the dynamic model, IMU, and electric sense to explore the contributing factors of the localization methods. Finally, to fully verify our proposed electric sense-based scheme, we conduct four types of localization experiments, including the very complicated scenario of the kidnapped robot problem. Three typical electric-emitter architectures are compared in these experiments, and we find that architectures with orthogonal features are stable in four localization scenarios. Our study provides a novel solution to the localization of autonomous underwater vehicles

with limited payload and also helps provide insights into large-scale underwater localization.

Acknowledgment

This work was supported in part by the National Natural Science Foundation of China under Grant 61973007 and in part by the Southern Marine Science and Engineering Guangdong Laboratory (Guangzhou) under Grant K19313901. The corresponding author is Chen Wang. This article has supplementary downloadable material available at https://doi.org/10.1109/MRA.2022.3202432, provided by the authors.

References

[1] A. M. Yazdani, K. Sammut, O. Yakimenko, and A. Lammas, "A survey of underwater docking guidance systems," *Robot. Auton. Syst.*, vol. 124, p. 103,382, Feb. 2020, doi: 10.1016/j.robot.2019.103382.

[2] M. A. Gibbs, "Lateral line receptors: Where do they come from developmentally and where is our research going?" *Brain Behav. Evol.*, vol. 64, no. 3, pp. 163–181, Feb. 2004, doi: 10.1159/000079745.

[3] S. Coombs, H. Bleckmann, R. R. Fay, and A. N. Popper, *The Lateral Line System*. New York, NY, USA: Springer Science & Business Media, 2014.

[4] C. Hopkins, "Electrical perception and communication," *Encyclopedia Neurosci.*, vol. 3, pp. 813–831, Dec. 2009, doi: 10.1016/B978-008045046-9.01827-1.

[5] I. Mahon, S. B. Williams, O. Pizarro, and M. Johnson-Roberson, "Efficient view-based SLAM using visual loop closures," *IEEE Trans. Robot.*, vol. 24, no. 5, pp. 1002–1014, Oct. 2008, doi: 10.1109/TRO.2008.2004888.

[6] A. A. Caputi, "The bioinspiring potential of weakly electric fish," *Bioinspiration Biomimetics*, vol. 12, no. 2, p. 25,004, Feb. 2017, doi: 10.1088/1748-3190/12/2/025004.

[7] J. R. Solberg, K. M. Lynch, and M. A. MacIver, "Active electrolocation for underwater target localization," *Int. J. Robot. Res.*, vol. 27, no. 5, pp. 529–548, May 2008, doi: 10.1177/0278364908090538.

[8] Y. Bai, J. B. Snyder, M. Peshkin, and M. A. MacIver, "Finding and identifying simple objects underwater with active electrosense," *Int. J. Robot. Res.*, vol. 34, no. 10, pp. 1255–1277, Apr. 2015, doi: 10.1177/0278364915569813.

[9] S. Lanneau, F. Boyer, V. Lebastard, and S. Bazeille, "Model based estimation of ellipsoidal object using artificial electric sense," *Int. J. Robot. Res.*, vol. 36, no. 9, pp. 1022–1041, Jun. 2017, doi: 10.1177/0278364917709942.

[10] V. Lebastard, C. Chevallereau, A. Girin, N. Servagent, P.-B. Gossiaux, and F. Boyer, "Environment reconstruction and navigation with electric sense based on a Kalman filter," *Int. J. Robot. Res.*, vol. 32, no. 2, pp. 172–188, Feb. 2013, doi: 10.1177/0278364912470181.

[11] K. D. Dimble, J. M. Faddy, and J. S. Humbert, "Electrolocation-based underwater obstacle avoidance using wide-field integration methods," *Bioinspiration Biomimetics*, vol. 9, no. 1, p. 016012, Jan. 2014, doi: 10.1088/1748-3182/9/1/016012.

[12] F. Boyer, V. Lebastard, C. Chevallereau, S. Mintchev, and C. Stefanini, "Underwater navigation based on passive electric sense: New perspectives for underwater docking," *Int. J. Robot. Res.*, vol. 34, no. 9, pp. 1228–1250, May 2015, doi: 10.1177/0278364915572071.

[13] J. Zheng, C. Huntrakul, X. Guo, C. Wang, and G. Xie, "Electric sense based pose estimation and localization for small underwater robots," *IEEE Robot. Automat. Lett.*, vol. 7, no. 2, pp. 2835–2842, Apr. 2022, doi: 10.1109/LRA.2022.3145094.

[14] M. Porez, V. Lebastard, A. J. Ijspeert, and F. Boyer, "Multi-physics model of an electric fish-like robot: Numerical aspects and application to obstacle avoidance," in *Proc. 2011 IEEE/RSJ Int. Conf. Intell. Robots Syst. (IROS)*, pp. 1901–1906, doi: 10.1109/IROS.2011.6094636.

[15] S. Mintchev et al., "An underwater reconfigurable robot with bio-inspired electric sense," in *Proc. 2012 IEEE Int. Conf. Robot. Automat. (ICRA)*, pp. 1149–1154, doi: 10.1109/ICRA.2012.6224956.

[16] D. J. Griffiths, *Introduction to Electrodynamics*, 4th ed. Cambridge, U.K.: Cambridge Univ. Press, 2017.

[17] T. Li, M. Bolic, and P. M. Djuric, "Resampling methods for particle filtering: Classification, implementation, and strategies," *IEEE Signal Process. Mag.*, vol. 32, no. 3, pp. 70–86, May 2015, doi: 10.1109/MSP.2014.2330626.

[18] T. I. Fossen, *Guidance and Control of Ocean Vehicles*. New York, NY, USA: Wiley, 1994.

[19] M. Rubagotti, P. Patrinos, and A. Bemporad, "Stabilizing linear model predictive control under inexact numerical optimization," *IEEE Trans. Autom. Control*, vol. 59, no. 6, pp. 1660–1666, Jun. 2014, doi: 10.1109/TAC.2013.2293451.

[20] S. Thrun, W. Burgard, and D. Fox, *Probabilistic Robotics*. Cambridge, MA, USA: MIT Press, 2006.

[21] J. Zheng, T. Zhang, C. Wang, M. Xiong, and G. Xie, "Learning for attitude holding of a robotic fish: An end-to-end approach with sim-to-real transfer," *IEEE Trans. Robot.*, vol. 38, no. 2, pp. 1287–1303, Apr. 2022, doi: 10.1109/TRO.2021.3098239.

Junzheng Zheng, State Key Laboratory for Turbulence and Complex Systems, Intelligent Biomimetic Design Lab, College of Engineering, Peking University, Beijing 100871 China. E-mail: zhengjunzheng@pku.edu.cn.

Jingxian Wang, Center for Robotics and Biosystems, Northwestern University, IL 60208 USA. E-mail: jingxianwang2026@u.northwestern.edu.

Xin Guo, State Key Laboratory for Turbulence and Complex Systems, Intelligent Biomimetic Design Lab, College of Engineering, Peking University, Beijing 100871 China. E-mail: guoxin@stu.pku.edu.cn.

Chayutpon Huntrakul, State Key Laboratory for Turbulence and Complex Systems, Intelligent Biomimetic Design Lab, College of Engineering, Peking University, Beijing 100871 China. E-mail: chayutpon@pku.edu.cn.

Chen Wang, National Engineering Research Center of Software Engineering, Peking University, Beijing 100871 China; State Key Laboratory for Turbulence and Complex Systems, Intelligent Biomimetic Design Lab, College of Engineering, Peking University, Beijing 100871 China. E-mail: wangchen@pku.edu.cn.

Guangming Xie, State Key Laboratory for Turbulence and Complex Systems, Intelligent Biomimetic Design Lab, College of Engineering, Peking University, Beijing 100871 China; Southern Marine Science and Engineering Guangdong Laboratory (Guangzhou), Guangzhou 511458 China. E-mail: xiegming@pku.edu.cn.